# Near-atomic cryo-EM structure of PRC1 bound to the microtubule

Elizabeth H. Kellogg[a,b,1], Stuart Howes[c,1,2], Shih-Chieh Ti[d], Erney Ramírez-Aportela[e], Tarun M. Kapoor[d], Pablo Chacón[e], and Eva Nogales[a,b,f,g,3]

[a]Molecular Biophysics and Integrative Bioimaging Division, Lawrence Berkeley National Laboratory, Berkeley, CA 94720; [b]Howard Hughes Medical Institute, University of California, Berkeley, CA 94720; [c]Biophysics Graduate Group, University of California, Berkeley, CA 94720; [d]Laboratory of Chemistry and Cell Biology, The Rockefeller University, New York, NY 10065; [e]Department of Biological Physical Chemistry, Rocasolano Physical Chemistry Institute, Consejo Superior de Investigaciones Científicas, Madrid 28006, Spain; [f]California Institute for Quantitative Biosciences, University of California, Berkeley, CA 94720; and [g]Department of Molecular and Cell Biology, University of California, Berkeley, CA 94720

This contribution is part of the special series of Inaugural Articles by members of the National Academy of Sciences elected in 2015.

Contributed by Eva Nogales, June 30, 2016 (sent for review May 25, 2016; reviewed by Andreas Hoenger and Hernando Sosa)

**Proteins that associate with microtubules (MTs) are crucial to generate MT arrays and establish different cellular architectures. One example is PRC1 (protein regulator of cytokinesis 1), which cross-links antiparallel MTs and is essential for the completion of mitosis and cytokinesis. Here we describe a 4-Å–resolution cryo-EM structure of monomeric PRC1 bound to MTs. Residues in the spectrin domain of PRC1 contacting the MT are highly conserved and interact with the same pocket recognized by kinesin. We additionally found that PRC1 promotes MT assembly even in the presence of the MT stabilizer taxol. Interestingly, the angle of the spectrin domain on the MT surface corresponds to the previously observed cross-bridge angle between MTs cross-linked by full-length, dimeric PRC1. This finding, together with molecular dynamic simulations describing the intrinsic flexibility of PRC1, suggests that the MT–spectrin domain interface determines the geometry of the MT arrays cross-linked by PRC1.**

PRC1 | microtubules | cryo-EM | MAPs | cytoskeleton

Cells rely on the microtubule (MT) cytoskeleton to help organize organelles (1), control cellular morphology (2), provide mechanical stability (3, 4), and form the spindle apparatus used to segregate chromosomes during cell division (5–8). The diverse functions of MTs are made possible through the action of motors (i.e., kinesin and dynein) and nonmotor MT-associated proteins (MAPs) that tightly regulate the MT network. Some of these proteins act by binding directly to the ends of MTs, either to the highly dynamic plus end, such as the conserved end-binding proteins (9, 10), or to the minus end (11, 12). Other MT regulators, such as MAP1 and MAP2/Tau, bind along the MT lattice, stabilizing it and helping build parallel arrays, most notably in axons (13, 14). Members of the MAP65 family, which includes human protein regular of cytokinesis 1 (PRC1) and its budding yeast ortholog Ase1, form antiparallel MT arrays important for setting the spindle midzone and determining the location of the cytokinetic ring (8, 15–19). In addition to binding selectively to antiparallel MTs, PRC1 recruits other spindle-organizing factors and therefore is an essential component of the mitotic spindle (15, 20). Proper functioning of PRC1 requires cell-cycle–dependent localization and regulation. PRC1 contains two nuclear localization signals (NLSs) in its C-terminal domain (Fig. 1*A*) and is found almost exclusively in the nucleus during interphase (21–23). As the cell enters mitosis, PRC1 localizes to the spindle and becomes concentrated at the midzone by late anaphase (22), similar to observations for Ase1 (24). PRC1 is subject to phosphorylation by several cyclin–cyclin-dependent kinase (CDK) complexes (21) and together with kinesin-4 can regulate MT antiparallel overlap at the spindle midzone (20, 23, 25, 26).

Previous studies have identified that the dimerization domain of PRC1 is within the N-terminal domain (Fig. 1*A*) and that the primary MT binding region relies on a set of conserved residues within the central spectrin domain (PRC1-S) (15, 22, 26). However, the C-terminal domain (PRC1-C) also was found to contribute to the MT-binding activity (15), and the specific contacts made between the MT and PRC1 were unclear. We used cryo-EM to visualize a monomeric PRC1 construct containing the spectrin domain and the full C-terminal domain (PRC1-SC) bound to the MT. The near-atomic resolution of our cryo-EM reconstruction allowed us to build an atomic model into the density and to explain, at the single amino acid level, the key interactions between PRC1 and the MT surface. We also found that PRC1-SC promotes MT assembly for both dynamic and taxol-stabilized MTs, suggesting that PRC1-SC stabilizes the MT lattice in a manner distinct from that of taxol. We propose that the unstructured C-terminal domain of PRC1-SC likely forms electrostatic contacts with the neighboring protofilament, thereby accounting for the increase in binding affinity when this C-terminal domain is included. Additionally, we found that the binding mode of the spectrin domain of PRC1-SC dictates the cross-bridge angle between antiparallel, cross-linked MTs, and we further investigated the validity of such a model using MD simulations.

## Results

**Features of the PRC1–MT Cryo-EM Reconstruction.** Full-length PRC1 consists of four domains: a dimerization domain, a rod domain, a spectrin domain, and a C-terminal domain (Fig. 1*A*). The dimerization and rod domains are required to orient the spectrin and C-terminal domains at opposite ends of an extended homodimer

### Significance

**PRC1 (protein regulator of cytokinesis 1) is critical to cellular architecture through its interaction with microtubules to form antiparallel microtubule arrays, like those in the spindle midzone. Here, cryo-EM studies describe, in close to atomic detail, the interaction of PRC1 with the microtubule surface. Together with previous studies, our structure leads to a model of how PRC1 promotes the establishment of stable, higher-order microtubule arrays.**

---

Author contributions: E.H.K., S.H., and E.N. designed research; E.H.K., S.H., E.R.-A., and P.C. performed research; E.H.K., S.-C.T. and T.M.K. contributed new reagents/analytic tools; E.H.K, S.H., and E.N. analyzed data; and E.H.K., S.H., and E.N. wrote the paper.

Reviewers: A.H., University of Colorado; and H.S., Albert Einstein College of Medicine.

The authors declare no conflict of interest.

Data deposition: Atomic coordinates have been deposited in the Protein Data Bank (PDB ID code 5KMG). The cryo-EM reconstruction has been deposited in the Electron Microscopy Data Bank (accession code EMD-8266).

See Profile on page 9395.

[1]E.H.K. and S.H. contributed equally to this work.

[2]Present address: Department of Molecular Cell Biology, Leiden University Medical Center, 2333 ZC Leiden, The Netherlands.

[3]To whom correspondence should be addressed. Email: enogales@lbl.gov.

This article contains supporting information online at www.pnas.org/lookup/suppl/doi:10.1073/pnas.1609903113/-/DCSupplemental.

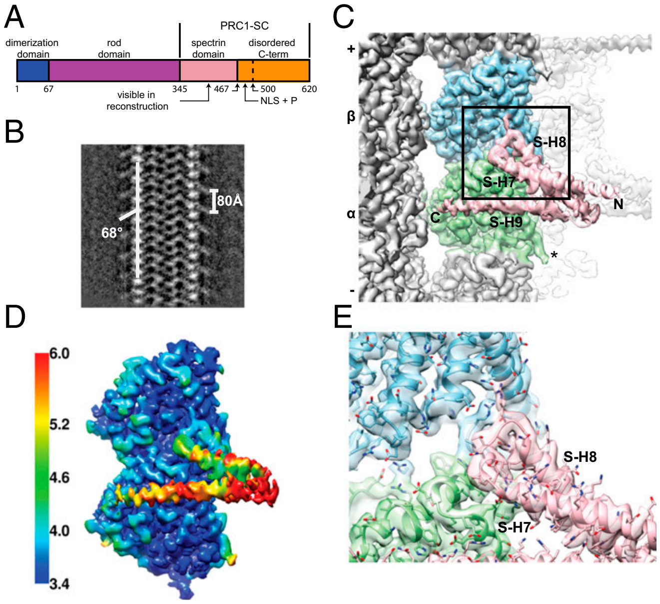

**Fig. 1.** The 4-Å resolution cryo-EM structure of the spectrin domain of PRC1 bound to the microtubule. (*A*) Domain structure of full-length PRC1 and of the PRC1-SC construct used in this study. Residues 470–500 contain the NLSs and phosphorylation sites (P). (*B*) 2D class average for an MT segment bound to PRC1-SC showing the ∼70° angle between the spectrin domain of PRC1 and the MT wall. (*C*) Side view of the cryo-EM reconstruction showing the bound PRC1 spectrin domain in pink and the tubulin dimer to which it is bound in green (α-tubulin) and blue (β-tubulin). The tail of α-tubulin is indicated by *. Although the construct used contains both the spectrin domain and C-terminal domain, only the spectrin domain (residues 345–467) is visible. (*D*) Segmented cryo-EM density map of the asymmetric unit, PRC1-SC bound to a tubulin dimer, displaying local resolution estimation. (*E*) Close-up of the box in *C* showing the density map and the atomic models for the spectrin domain of PRC1 (pink) and α- and β-tubulin (green and blue, respectively).

and for PRC1's cross-linking and bundling of MTs (15). MT bundling would result in MT images that cannot be processed because of overlap; therefore, to obtain a reconstruction with the highest possible resolution, we chose to focus on the PRC1-SC construct consisting of only the spectrin and C-terminal domains (Fig. 1*A*), which are the MT-binding regions. Raw images showed MT binding by PRC1-SC (Fig. S1*A*), and 2D class averages display clear density corresponding to PRC1-SC decorating the MT lattice with an ∼80-Å repeat (i.e., binding once per αβ-tubulin dimer) (Fig. 1*B* and Fig. S1*B*). Using ∼230,000 tubulin heterodimers, corresponding to 17,069 overlapping MT segments (*Materials and Methods*), we generated a 3D reconstruction of an MT with bound PRC1-SC with an overall resolution better than 4 Å (Fig. 1 and Fig. S1*C*). The final density map (Fig. 1*C*) shows high-resolution features corresponding to α-helical register, β-strand separation, and side-chain densities for larger amino acids (Fig. 1 and Fig. S2), as expected for a nearly atomic-resolution cryo-EM map. However, local resolution estimation reports a range of resolutions throughout the density map that reflects conformational or compositional heterogeneity (Fig. 1*D*). The resolution for tubulin is generally between 3.4 and 4 Å, but the resolution for the PRC1-SC molecule is lower, in the range of 3.8–6 Å, and is progressively poorer as the radius becomes larger, i.e., as the molecule becomes more distant from its contact with the MT surface. This lower resolution could be caused by two different factors: PRC1-SC occupancy on the MT and/or its flexibility. We therefore attempted to quantify the percentage of tubulin-binding sites occupied by PRC1-SC on the MT lattice. Because PRC1-SC recognizes a single binding site per tubulin heterodimer, and tubulin dimers are regularly spaced at ∼80 Å along the MT lattice, the repeating pattern of PRC1-SC binding will contribute to the intensity of a layer line in Fourier space corresponding to that distance (i.e., ∼1/80 Å$^{-1}$). Note that this layer line is very weak for naked MTs without a "decorating" binding factor because of the similarity between α- and β-tubulin. By comparing the intensity of this layer line (and higher orders) in our final reconstruction with the layer lines obtained from a simulated map containing full PRC1-SC decoration (27, 28) (*Materials and Methods*), we estimate that PRC1-SC occupied ∼49% of all possible MT-binding sites in the MT images used for the reconstruction (Fig. 1 and Fig. S1*D*). Thus, this "compositional" heterogeneity (i.e., partial occupancy) must be a factor contributing to the comparatively lower resolution of PRC1-SC as compared with tubulin. However, we suspect that conformational heterogeneity also may contribute to this disparity. Although the local resolution for PRC1-SC is highest (3.8 Å) at the point of interaction with tubulin, it is noticeably lower (5–6 Å) near the N and C termini. In fact, the density for the C-terminal domain beyond residue 467 (the end of the spectrin domain) is not visible in our high-resolution map. We reasoned that although the C-terminal domain may not adopt a single, well-defined structure, it could adopt a limited range of compact conformations that would be observable at 10- to 20-Å resolution. However, even low-pass filtering the reconstruction to this resolution did not reveal any additional density attributable to this domain, confirming predictions based on results from Phyre2 (29) and META-Disorder (30) that PRC1's C terminus is disordered.

In the reconstruction we can clearly identify the fold of the PRC1 spectrin domain (PRC1-S), consisting of a three-helix bundle (Fig. 1*C*) of helices [S-H7, S-H8, and S-H9, following previous nomenclature (26)]. Furthermore, the previously reported crystal structure (15, 26) fits well within the observed density. In a previous cryo-EM reconstruction of PRC1-SC limited to ∼20-Å resolution, docking of the crystal structure suggested that the PRC1 spectrin domain was at an ∼90° angle with respect to the MT surface (15). In contrast, both our 2D class averages (Fig. 1*B* and Fig. S1*B*) and our high-resolution 3D reconstruction (Fig. 1*C*) clearly show that PRC1-SC projects from the MT surface at an angle of ∼70°. Interestingly, previous tomographic studies reported a 70° cross-bridge angle between antiparallel MTs cross-linked by full-length PRC1 (i.e., PRC1 including the N-terminal dimerization domain) (15). Our present work now indicates that the cross-bridge angle does in fact originate from the orientation of the spectrin domain with respect to the MT lattice.

**Molecular Basis of PRC1-SC Binding Specificity.** To understand the atomic details of the MT–PRC1-SC interaction, we generated an atomic model of PRC1-SC bound to tubulin using previous atomic models of PRC1 (15) and the MT (27) as starting points. From these initial models, we retraced and refined the atomic coordinates to fit the final density map better, using methods optimally suited for near-atomic (4 Å or better) cryo-EM reconstructions (*Materials and Methods*). In particular, the loop between S-H7 and S-H8 (residues 374–384, from now on referred to as S-H7H8 loop) was either absent or involved in crystal contacts in the previously determined crystal structures (15, 26), necessitating de novo loop-tracing. The presence of clear density for this region in our reconstruction supports the idea that the S-H7H8 loop is likely disordered in solution but becomes ordered upon binding to the MT lattice. Our resulting atomic structure shows how the spectrin domain binds at the intradimer interface along a protofilament. Interactions with tubulin involve primarily the S-H7H8 loop (Figs. 1*E* and 2 *A* and *B*) [notice that side-chain densities for negatively charged residues are missing from cryo-EM density maps, likely because of radiation damage during early electron exposure (31)], with additional contacts made through S-H9 (Fig. 2*C*). The S-H7H8 loop makes a critical contact with helix H12 in β-tubulin. R381 in PRC1-S interacts with N424 in β-tubulin and potentially with D427 (Fig. 2*A*). Additionally, N380 in PRC1-S is well positioned (3 Å between donor and acceptor atoms) to hydrogen bond with

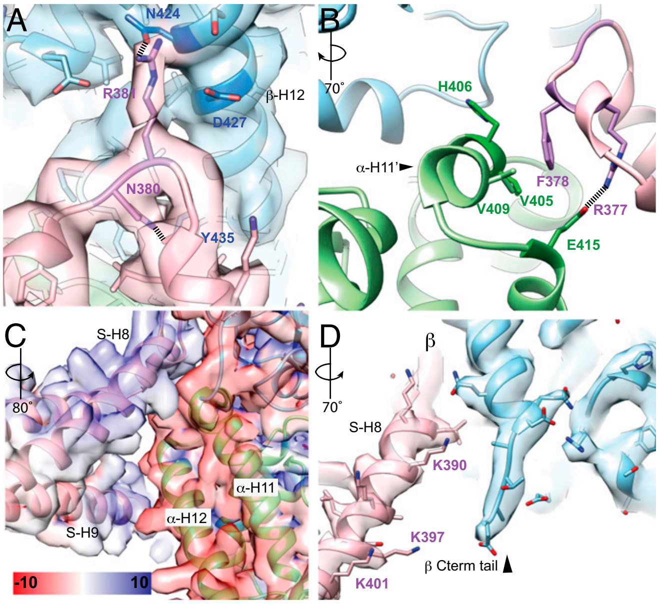

**Fig. 2.** Model of PRC1–tubulin interactions. (*A*) R381 and N380 in the loop between helices S-H7 and S-H8 of PRC1-SC (pink) are positioned to contact D427, N424, and Y435 in the H12 helix of β-tubulin (blue). (*B*) F378 of PRC1-SC nestles into a hydrophobic pocket formed by V405 and V409 in α-tubulin (green), and R377 of PRC1-SC likely contacts E415 of α-tubulin. (*C*) Helix H9 of PRC1-SC forms a complementary electrostatic surface with tubulin (the colored surface shown corresponds to the atomic model). Helix H9 is rich in basic residues (blue), whereas tubulin surface in its close proximity is negatively charged. Electrostatic units are $k_bT/e^-$. (*D*) Part of the β-tubulin tail is structured in our MT–PRC1-SC reconstruction, likely as a result of its stabilization by interactions with the multiple lysines (K390, 397, 401) in S-H8 of PRC1. All rotations for the views displayed in *B*–*D* are relative to the orientation shown in *A*.

β-tubulin's Y435 (Fig. 2*A*). F378 in PRC1-S nestles into a hydrophobic pocket in α-tubulin formed by V405 and V409 (within the segment connecting α-H11 and α-H12, denoted "α-H11′") (Fig. 2*B*). Additionally, R377 in PRC1-S is positioned to form a salt bridge with E415 in α-tubulin (within H11) (Fig. 2*B*).

Although S-H9 lies over the α-tubulin subunit, only its C-terminal portion is within interacting distance of α-H12 (Fig. 2*C*). The position of S-H9 and the abundance of basic residues across homologs in this region (residues 439–456) (Fig. S3) suggest that S-H9 interacts via electrostatic interactions with negative charges on the nearby MT surface.

The acidic C-terminal tails of tubulin are generally unstructured and, with a few notable exceptions, are not visible in most MT cryo-EM reconstructions (32, 33). It is thus noteworthy that we can clearly trace up to five extra amino acids from the last residue seen in previous cryo-EM studies (27, 34) for both α- and β-tubulin (Figs. 1*C* and 2*D*). The length and conformation of the tubulin tails we see here are similar to previous reports of structured tubulin tails (32, 33) indicating that the tubulin tails become partially structured upon PRC1-SC binding. The β-tubulin tail is near lysines K390, K397, and K401 on the surface of S-H8. The α-tubulin tail, in contrast, has no structured PRC1-SC density in close contact (Fig. 1*C*). However, the C terminus of PRC1-S is ∼30 Å from the C-terminal tail of α-tubulin, placing it within an appropriate range to interact with the disordered C-terminal domain of PRC1-SC (which comprises >100 amino acids). Together, these features suggested that PRC1-SC binding could be mediated in part by the tubulin tails.

Because of the importance of PRC1 in mitosis, it is reasonable to assume that residues critical for MT binding should be well conserved across species. To gauge the importance of the ascribed PRC1-S–tubulin interactions, we aligned several PRC1 sequences across a diverse set of eukaryotes and mapped the conservation onto our atomic model (Fig. S3). We find that the described critical interactions (displayed as spheres) correspond well to highly conserved residues. PRC1-S residues R377, F378, N380, and R381, observed to make direct contacts with tubulin, are 100% conserved in all examined homologs ranging from yeast to human. Residue K390, positioned to interact with the C-terminal tubulin tail, is also highly conserved and is followed by a conserved stretch of positively charged residues, supporting our proposal that basic residues in this region are required to interact with tubulin's acidic C-terminal tail. These observations are further supported by alanine mutagenesis showing that residues R377, R381, and K390 contribute significantly to PRC1-S's MT-binding activity (15). Some residues that are highly conserved but do not participate in PRC1-S–tubulin interactions appear to play a supportive structural role (e.g., PRC1-S E388 hydrogen bonds with R377, which in turn interacts with α-tubulin E415). The residues in helix S-H9 (439–456) are less conserved than the S-H7H8 loop but maintain general basic character, supporting our model in which S-H9 makes electrostatic interactions with the acidic MT surface.

**Molecular Basis of PRC1-SC's Specificity for the Intradimer Interface.** Each PRC1-SC binds the MT specifically at an intradimer interface (within an αβ-tubulin heterodimer), using a small footprint on the tubulin surface that is significantly conserved between α- and β-tubulin (∼70% overall). The calponin homology (CH) domain of Ndc80, a kinetochore component, also binds tubulin using a very small region of the MT surface. In that case, the conservation of the tubulin-binding site between α- and β-tubulin is so significant that human Ndc80 also binds at the interdimer interface, where the α- and β-tubulin segments of the footprint are swapped with respect to those in the intradimer contact (35, 36). Thus, we decided to investigate the basis of PRC1-SC's specificity for the intradimer over the equivalent interdimer interface. Although the residues involved in contact with PRC1-S are generally conserved in α- and β-tubulin, a number of notable exceptions may explain the observed specificity (Fig. 3*A*): (*i*) β-tubulin D427, which is close to PRC1-S R381, is substituted at the interdimer interface by α-tubulin A427, thus disrupting a likely salt bridge; (*ii*) β-tubulin Y435, which hydrogen bonds with PRC1-S N380, corresponds to V435 in α-tubulin at the interdimer interface; (*iii*) the hydrophobic tubulin pocket filled by PRC1-S F378 at the intradimer interface is disrupted in the interdimer interface by the presence of a polar residue, β-tubulin T409 (in place of α-tubulin V409 at the intradimer interface) (Fig. 3*B*). Finally, α-tubulin G416, whose small size allows PRC1-S R450 to interact with neighboring charged amino acids (α-tubulin E414 and α-tubulin E420), is substituted by β-tubulin M416 and likely sterically occludes PRC1-S R450 from interacting with these residues at the interdimer interface (Fig. 3*C*). We propose that these critical sequence changes between α- and β-tubulin both sterically and chemically confer PRC1's selectivity for the tubulin intradimer interface.

**PRC1's Disordered C-Terminal Domain Forms Electrostatic Interactions with the Neighboring Protofilament.** In our reconstruction, the C-terminal domain beyond residue 467 is not visible, verifying that it has no regular structure (see *Features of the PRC1-MT Cryo-EM Reconstruction*). However, the reconstruction shows that the end of S-H9, which precedes the C-terminal domain, is oriented so that the C-terminal domain of PRC1-SC could interact with a neighboring α-subunit close to α-H3. Electrostatic maps, computed using the Adaptive Poisson–Boltzmann Server (37), reveal that the site in the neighboring protofilament, potentially adjacent to the C terminus of PRC1 (i.e., α-H11 and the loop connecting α-H9 and α-S8), is negatively charged (Fig. 4), further suggesting that it forms a complementary electrostatic surface for the predominantly positively charged C-terminal domain of PRC1. The lack of density for the C-terminal domain means it does not make

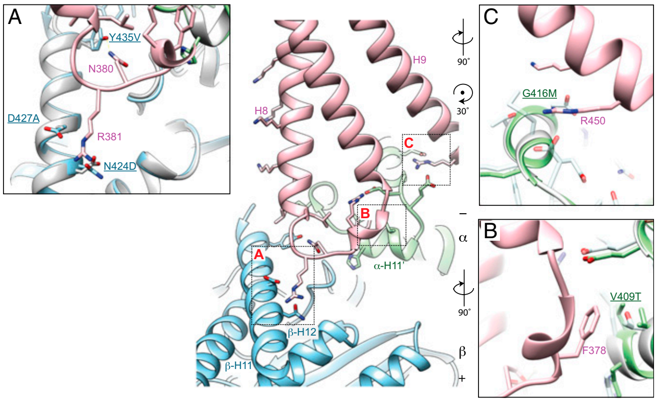

**Fig. 3.** Molecular basis for the specificity of PRC1-SC for the intradimer interface. A number of critical PRC1-S–tubulin contacts are present only at the intradimer interface. PRC1-S–tubulin in the center panel is rotated 180° in-plane from the view shown in Fig. 2*A*, and the MT is tilted out of plane to be viewed from the plus end of the microtubule. (*A*) β-Tubulin D427 at the intradimer site corresponds to α-tubulin A427 at the interdimer site, eliminating electrostatic interactions with R381 in PRC1. β-Tubulin Y435 is α-tubulin V435 at the interdimer site, which eliminates hydrogen bonding to N380 in PRC1-S. (*B*) α-Tubulin V409 is β-tubulin T409 at the interdimer site, reducing the hydrophobicity of the tubulin pocket that cradles PRC1-S F378. (*C*) α-Tubulin G416 is β-tubulin M416 at the interdimer site, potentially occluding PRC1-S R450 sterically from interacting with tubulin.

specific contacts with the MT, indicating instead that it can make multiple interactions to increase the affinity of PRC1-SC for MTs. Because the interface between PRC1-S and tubulin is relatively small (~500 Å$^2$), the C terminus would provide favorable interactions to target PRC1-SC to the MT lattice and could increase PRC1-SC's binding affinity for MTs.

**PRC1-SC Promotes MT Assembly.** The results of our electrostatic calculations lead to the prediction that PRC1-SC should facilitate MT assembly by bridging across protofilaments. We tested whether PRC1-SC enhances MT assembly by performing cosedimentation assays. PRC1-SC and MTs were mixed together, and the reaction mixtures were centrifuged to separate large complexes (i.e., MTs and bound proteins) from unbound, soluble proteins (i.e., unpolymerized tubulin and unbound PRC1-SC) to determine how the proteins partitioned between the pellet and supernatant fractions (*Materials and Methods*).

Under our experimental conditions, PRC1-SC self-pellets to some extent (Fig. 5 *A* and *B*, lanes PRC1), but most of the protein remains in the supernatant fraction. When using dynamic MTs and substoichiometric amounts of PRC1-SC, we observed significantly greater MT assembly in the presence of PRC1-SC, as shown by the increase in the amount of tubulin in the pellet fractions and a corresponding decrease in the supernatant fractions (Fig. 5 *A* and *B*, lanes MTs and MTs+PRC1-SC). To replicate better the sample conditions that we imaged, we performed the experiment with taxol-stabilized MTs at much lower concentrations of MTs (as allowed by this stabilizing drug) and with a molar excess of PRC1-SC. We again observed an increase in MT assembly in the presence of PRC1-SC (Fig. 5 *C* and *D*, lanes TMTs and TMTs+PRC1).

Based on the presence of density for the C-terminal tails of αβ-tubulin in our reconstruction (Fig. 2*D*), we also tested whether these tails contributed to PRC1-SC binding and if they were required for PRC1-SC to promote MT assembly. MTs were assembled and then treated with subtilisin to cleave the C-terminal tails of tubulin (38). A similar amount of PRC1-SC bound to both native and subtilisin-cleaved MTs (Fig. S4 *A* and *B*), clearly indicating that, at least at the concentrations used for this study, the C-terminal tails of tubulin do not contribute significantly to the apparent binding affinity of PRC1-SC. Concerning PRC1 promotion of tubulin assembly, an increase in tubulin polymerization was observed in the presence of PRC1-SC for both the dynamic subtilisin-treated MTs (Fig. S4 *A* and *B*) and the taxol- and subtilisin-treated MTs (Fig. S4 *C* and *D*) similar to that observed for full-length tubulin. [Notice that subtilisin-treated MTs polymerize to a greater extent than untreated MTs, as reported previously (39).] This result indicates that the C-terminal tails of tubulin are not needed for PRC1-SC promotion of MT assembly, at least under the conditions we tested.

**Kinesin, Dynein, and PRC1 Partially Share a Tubulin-Binding Site.** PRC1 is not the only protein that has been found to bind to MTs by recognizing the tubulin intradimer interface (see ref. 40 for a recent review). In particular, the MT-interacting domains of the motors dynein and kinesin are both known also to bind across the tubulin intradimer interface. Specifically, the H11′ connection between the C-terminal α-H11 and α-H12 has been previously identified as a major part of the binding interface for both the kinesin motor head (41, 42) and the dynein MT-binding domain (MTBD) (43). This tubulin region is near the site where we observe the S-H7H8 loop in PRC1-S interacting with tubulin. To investigate whether there are specific residues in tubulin that are shared in the interaction with kinesin, PRC1, and dynein, we performed sequence and structural alignments for these proteins, using tubulin as the common element to superimpose the MT-MAP models (*Materials and Methods*). Although as yet there is no atomic-resolution information on the binding of the dynein MTBD to MTs, hybrid models of this interaction have been generated by integrating diverse sources of data, including crystal structures (41–47), medium-resolution EM maps (43, 47), and biochemical data (48, 49). Superposition of the MT–kinesin atomic model with our MT–PRC1-SC atomic model identified kinesin R278 and PRC1 R381 as functionally similar in their interaction with tubulin (potentially with β-tubulin D420 and β-tubulin E427) (Fig. 6*A*). Superposition of the MT–dynein MTBD model with our MT–PRC1-SC model revealed that dynein has two lysine residues (dynein K3298 and dynein K3299) in a position approximately equivalent to PRC1 R381, one of which may interact with tubulin in a similar manner (Fig. 6*B*). Previous mutational analyses identified these dynein residues as critical to the dynein–tubulin interaction (48). To identify additional residues that may be important for the interaction of tubulin with these motors, we chose a 4.0-Å cutoff for the distance between tubulin and the binding partner to inspect potential contacts (dark green residues in Fig. 6). α-Tubulin H406 and α-tubulin V409, within the same hydrophobic pocket, are both within range potentially

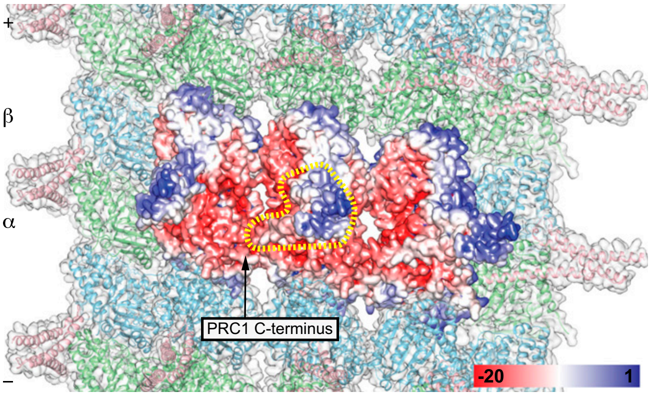

**Fig. 4.** Electrostatic map of three PRC1-SCs bound to three tubulin dimers in adjacent protofilaments. The positively charged, unstructured C terminus of PRC1-SC (composed primarily of arginine and lysine) is positioned to form complementary electrostatic interactions with the negatively charged (red) tubulin surface. The dashed yellow line outlines PRC1-S. Electrostatic units are $k_bT/e^-$.

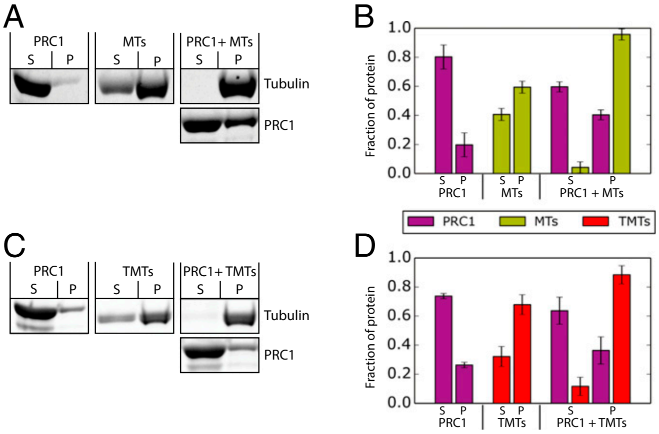

**Fig. 5.** PRC1 promotes tubulin polymerization of dynamic and taxol-stabilized MTs. SDS/PAGE analysis of cosedimentation assays showing supernatant (S) and pellet (P) fractions for PRC1-SC bound to dynamic MTs at 10 μM and PRC1-SC at 5 μM (*A*) (quantitation in *B*) and taxol-stabilized MTs (TMTs) at 2 μM and PRC1-SC at 10 μM (*C*) (quantitation in *D*). Quantitations in *B* and *D* are from three experiments; error bars indicate the SD. The increased tubulin in the pellet fractions in the presence of PRC1-SC, for both dynamic and taxol-stabilized MTs, reflects the increase in tubulin polymerization. Notice that the tubulin concentration used for dynamic MTs is fivefold higher than that used for taxol-stabilized MTs.

to interact with the kinesin motor head and the dynein MTBD as well as with PRC1-S (Fig. 2*B*). α-Tubulin G416, which in our atomic model is close enough to interact with PRC1 R450 (Fig. 3*C*), also has been shown to make contact with kinesin K237 (41). Furthermore, we observed that residues β-tubulin R264, on the loop between β-tubulin H8 and β-tubulin S7, and β-tubulin Q434, on β-tubulin H12, are both potentially shared as binding partners by PRC1 and the loop L12 on kinesin that is sensitive to the nucleotide state within this motor (45, 46, 50, 51). In summary we find that G416 on H12 of α-tubulin is part of the interaction surface with both kinesin and PRC1-SC and that N424 and D427 on β-tubulin, also on H12, are shared interacting residues with kinesin, PRC1, and dynein. The region connecting H11 and H12 on α-tubulin forms a hydrophobic pocket defined by residues α-tubulin V405 and α-tubulin V409 that also interacts with all three of these binding partners, indicating that these tubulin motifs constitute a generally recognized platform for MT-binding proteins that makes simultaneous interaction within the same tubulin subunit impossible.

**PRC1 Adopts an Extended Conformation and a Range of Spectrin Orientations.** Inspection of the previously reported X-ray crystallographic structure of PRC1 (26) reveals that the orientation of the two spectrin domains is not antiparallel and therefore is incompatible with antiparallel MTs cross-linked by full-length PRC1 (Fig. 7). Given that the observed cross-bridge angle from tomographic reconstructions (15) coincides with the angle we observed between the PRC1 spectrin domain and the MT, we sought to determine whether molecular dynamics (MD) simulations of the PRC1 crystal structure would suggest that the spectrin domains could rearrange appropriately for antiparallel cross-linking to MTs. We first investigated the intrinsic flexibility of the PRC1 homodimer using large-scale atomic simulations starting with the crystallographic structure (26). The bent-rod shape of the crystallographic structure was rapidly relaxed in our simulations, revealing the high flexibility of the molecule (Fig. 8 and Movie S1). In both our simulations, PRC1 quickly adopts an extended but quite flexible conformation. The extension that accompanies relaxation of the crystallographic structure can be observed by monitoring the distance between the tips of the spectrin domains as the simulation proceeds in time. The distance between the PRC1 tips, as measured by the Cα–Cα distance between two threonines located at each end of the PRC1 homodimer (furthest away from the N-terminal dimerization domain) (Fig. 8*A*), increased from 31.7 nm in the initial conformation to an equilibrium distance around 39.5 nm (Fig. 8*C*).

This extended conformation is nevertheless still quite flexible, as previously described (15). Flexible joints, located mainly at loop regions of the rod domain, allow the movement of rigid structural modules within PRC1, including the dimerization domain and the junction between the rod and spectrin domains (Figs. S5 and S6). As a result of this flexibility, the spectrin domains rotate significantly with respect to each other during the course of two large-scale independent simulations (Fig. 8*D* and Fig. S5). However, the molecule is partially constrained toward configurations in which the spectrin domains point in opposite directions. The torsional

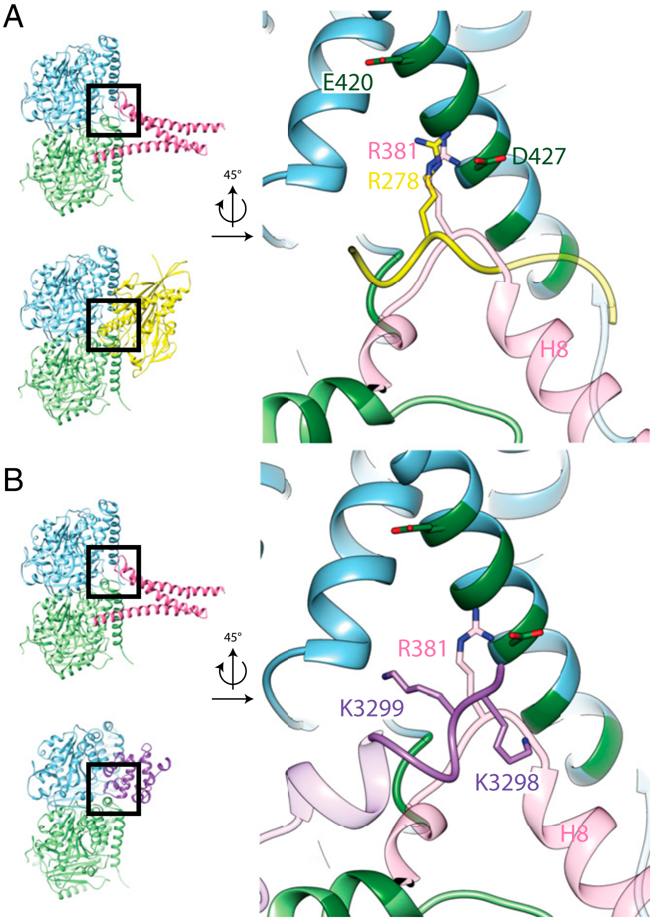

**Fig. 6.** The binding site of PRC1 on tubulin partially overlaps with that of kinesin and the MTDB of dynein. (*A*) Comparison between the binding site of PRC1-S and the motor domain of kinesin. Shown are side views of a tubulin dimer bound to PRC1-S (*Upper Left*) and the kinesin motor domain (*Lower Left*). The squares mark the binding site shown in more detail on the right. Part of the kinesin structure near loop L12 (yellow) corresponds to the loop in PRC1-S that engages tubulin and shares with it a conserved arginine. Side chains are shown for the tubulin residues D427 and E420 that stimulate kinesin ATPase activity (51). (*B*) Comparison between the binding site of PRC1-S and the MTBD of dynein. Shown are side views of a tubulin dimer bound to PRC1-S (*Upper Left*) and dynein's MTBD (*Lower Left*). The squares mark the binding site shown in more detail on the right. (*Right*) Superposition of the binding sites of PRC1-S and the dynein MTBD on tubulin. The relevant part of the dynein MTBD is shown in gray. Side chains for lysine residues on dynein that occupy a position similar to that of R381 in PRC1-S are shown. In all panels, α-tubulin is shown in light green, β-tubulin is shown in light blue, and PRC1 is shown in pink.

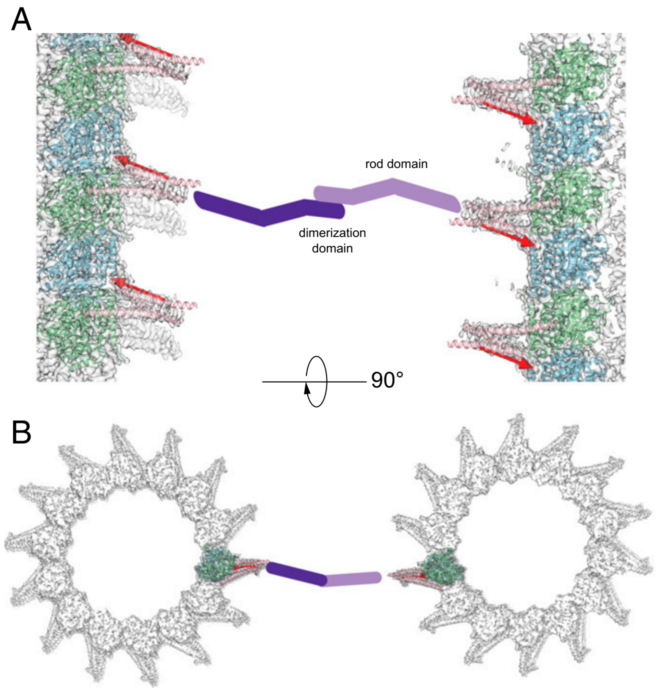

**Fig. 7.** The spectrin domain is oriented to interact preferentially with antiparallel microtubules. Atomic models of αβ-tubulin and PRC1-SC (green, blue, and pink, respectively) for one protofilament are docked into the full-density maps (gray). The dimerization and rod domains are shown as cartoons in two purple hues. The side view (*A*) and end-on view (*B*) of two antiparallel microtubules (spaced by 30 nm to reflect the spacing and cross-bridge angle experimentally observed in previous cryo-tomography studies of PRC1–cross-linked MTs) (15) show how the orientation of the spectrin domains promotes antiparallel microtubule cross-linking.

angle (Ω) defined by two planes, each containing a spectrin domain (Fig. 8*B*), starts at Ω ~ 50° in the crystallographic structure and can range from 30–210° (a torsional angle of 180° is required for the antiparallel arrangement of cross-linked MTs as displayed in Fig. 7), with values around 70–100° at equilibrium. Interestingly, conformations with spectrin domains pointing in the same direction (Ω = 0°) are not observed in our long-scale simulations, indicating that their relative orientation is partially constrained against parallel configurations. The conformational variability of the molecule, including the relative orientations of the spectrin domains, can be visualized directly in Movie S1. We argue that the natural tendency of PRC1 toward an elongated conformation, together with an antiparallel predisposition of the spectrin domains as observed in the simulations, agrees with previous tomographic data on PRC1-bundled MTs and supports the selectivity of PRC1 in cross-linking antiparallel MTs.

## Discussion

Using cryo-EM and atomic modeling, we have visualized the near-atomic details of the PRC1–MT interaction and thus have defined how PRC1 specifically recognizes the tubulin–intradimer interface. Critical specific interactions involve residues in the S-H7H8 loop of PRC1 that are nearly 100% conserved from yeast to human. In contrast to these specific contacts, helix S-H9, which is visualized in our study at lower resolution, likely because of intrinsic flexibility, uses a conserved basic character (i.e., lysine/histidine/arginine) for electrostatic interactions with the negative charge on the interacting surface of tubulin, which likely extends to the acidic C-terminal tails.

The specific contacts between PRC1 and tubulin identified by our atomic model are still likely to be insufficient to account for PRC1's binding affinity for MTs. Previous cosedimentation assays that measured the binding affinities of various PRC1 constructs for assembled MTs demonstrated that the spectrin domain alone (PRC1-S) has weak affinity for the MT lattice (15, 22). A fivefold increase in binding affinity for MTs is achieved by including the arginine/lysine-rich C-terminal disordered domain ($K_d$ ~ 3.3 μM for PRC1-S vs. 0.6 μM for PRC1-SC) (15). Despite the presence of nearly 100 residues beyond helix S-H9 in our construct, we do not see density for any of these residues, as is consistent with the previous proposal that the C-terminal domain of PRC1 is unstructured. Because of the orientation of PRC1's H9, which precedes the C-terminal domain, and as supported by electrostatic calculations, we propose that PRC1's disordered basic C terminus interacts with a negative patch on the neighboring protofilament to increase PRC1's binding affinity for the MT surface. Logical extension of this model dictates that, by binding across protofilaments, PRC1 should facilitate MT assembly. Indeed, our cosedimentation assays show that more tubulin polymerizes in the presence of PRC1-SC. Interestingly, PRC1 promotes the polymerization even in the presence of the potent MT-stabilizing drug taxol, detectably reducing the critical concentration of assembly in the presence of the drug. This result suggests that the action of PRC1-SC on MT assembly may involve a molecular mechanism different from that of taxol, making the effects additive.

The PRC1 C-terminal domain contains phosphorylation sites at T470 and T481 that are known substrates for cyclin–CDK and whose phosphorylation state is tightly coupled to the cell cycle (21, 22). When PRC1 is phosphorylated, its MT bundling activity is reduced (22), as is consistent with a model in which the negative charge of phosphate groups would disrupt the electrostatic interactions between tubulin and PRC1. The presence of a disordered region under phosphoregulation is commonly observed for other MT-binding proteins, such as Ndc80 (33), CENP-E (52), and Bim1 (53).

The surface of tubulin recognized by PRC1's S-H7H8 loop is partially shared by kinesin and the dynein MTBD. Strikingly, both PRC1 and kinesin position an absolutely conserved arginine to interact with conserved residues in β-tubulin H12. Although PRC1 and the motors kinesin and dynein all have a single binding site per tubulin dimer, at the intradimer interface, the CH domain of human Ndc80 within the Ndc80 kinetochore complex binds with double that stoichiometry at both the intra- and the interdimer interfaces (33, 35, 54). The Ndc80 CH lacks the arginine residue that may be important to determine the specificity for β-tubulin N424 (with which PRC1 R381 and kinesin R278 interact). Instead, residues such as the conserved glutamic acid E415, present in both α- and β-tubulin, and lysine/arginine residues on the C-terminal end

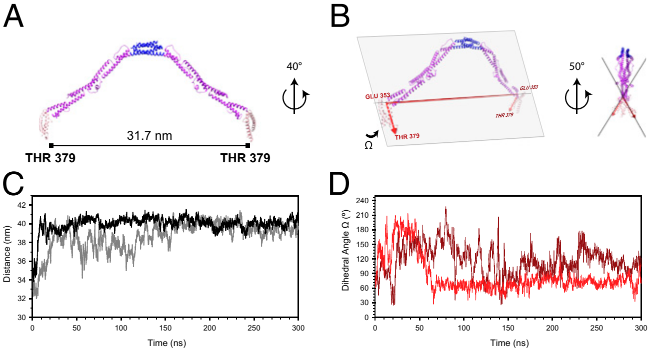

**Fig. 8.** Relaxation of the PRC1 dimer structure along the MD trajectories into an extended conformation. (*A*) Crystallographic structure of PRC1NSΔC with the Cα–Cα distance between two residues (T379) located in the L7 loop at both ends of the homodimer. (*B*) The dihedral angle (Ω) between the two spectrin domains monitored from the initial crystallographic conformation. (*C* and *D*) Time evolution of the distance (*C*) and angle Ω (*D*) during two independent MD simulations showing the distance increasing to a more extended conformation and the constrained angle fluctuating in the range of 70–100° at equilibrium.

of H11 for both α- and β-tubulin mediate critical interactions with Ndc80 at the intradimer and interdimer interfaces. Because several of the well-studied MT-binding proteins appear to recognize tubulin in overlapping regions of the MT surface (40), and given the sheer number of MT-binding proteins still to be characterized structurally and in their binding to tubulin, it is tempting to speculate that there are classes of MAPs that use defined sets of binding motifs and therefore compete with each other for MT real estate (40). This will be an important area for future cryo-EM–based structural studies.

We find that the spectrin domain of PRC1 binds to the MT surface at an ∼70° angle, pointing to the minus end. This angle is consistent with the angle of the cross-bridges between cross-linked MTs previously observed by cryo-electron tomography of MT–PRC1 bundles (15). Although initially this angle was attributed to the dimerization and rod domains, we find here that the geometry is determined by the orientation of the spectrin domain with respect to the MT lattice. The conformation of the full-length homodimer adopted in the reported crystal structure (26) is incompatible with the antiparallel arrangement that would be inferred from our model, and we hypothesize that this conformation likely results from the effect of crystal contacts on the dimer structure. Our MD simulations show that when the structure is allowed to relax unconstrained, it quickly adopts an even more extended configuration that exhibits a large degree of torsional flexibility. The equilibrium separation between the spectrin domains was consistent in both our simulations and is compatible with the $35 \pm 2$-nm spacing observed by tomography (15). Our simulations also revealed that the relative orientation of the spectrin domains is partially restricted to a range of 30–210°. The modular, restrained flexibility of the PRC1 molecule limits the range of preferred orientations of the spectrin domain, likely increasing the efficiency of MT capture and the antiparallel cross-linking of MTs while reducing the requirement for preexisting antiparallel MTs to establish a cross-bridge. On the other hand, the antiparallel binding orientation of the PRC1 spectrin domain (Fig. 7) and the conformations observed in the MD simulations of the PRC1 dimer help explain how PRC1 would selectively cross-link antiparallel MTs. In the spindle midzone, where multiple PRC1 molecules are present on each MT, the antiparallel bias of PRC1 dimers would accumulate to help arrange and stabilize regions of overlapping MTs. Furthermore, the ability of PRC1 to promote tubulin assembly likely contributes to the increased stability of the spindle midzone.

The findings of this work are summarized in Fig. 9. When bound to an MT, the spectrin domain of PRC1 adopts a fixed 70° angle with respect to the MT, but the rest of the dimer exhibits modular flexibility, increasing the tolerance for the possible orientations of the second MT when an initial cross-bridge is formed (Fig. 9*A*). When a second MT is bound, the preference for PRC1 to adopt antiparallel spectrin configurations would bias the antiparallel MT cross-linking (Fig. 9*B*). Binding of multiple PRC1 molecules would further steer the MTs into an antiparallel arrangement (Fig. 9*D*). Nevertheless, PRC1 remains flexible enough to bind with different protofilament registers on each MT. The spindle midzone is subject to many forces during mitosis (55) and PRC1's ability to promote polymerization (Fig. 9*C*) likely increases the stability of MTs that are critical for positioning the mitotic spindle as well as providing some degree of compliance.

## Materials and Methods

**Protein Purification.** All materials purchased from Sigma-Aldrich unless indicated otherwise. A sequence encoding a tobacco etch virus (TEV) protease site and a hexahistidine tag was fused to the 5′ end of PRC1-SC (amino acids 303–620). The overexpression of His$_6$-tagged PRC1-SC in BL21 (DE3) Rosetta cells was induced by 0.5 mM isopropyl β-d-1-thiogalactopyranoside at 18 °C for approximately 12–16 h. The following steps were done on ice or at 4 °C. We lysed cells in lysis buffer [50 mM phosphate buffer, 20 mM imidazole, 300 mM NaCl, 0.5% Tween-20, 1 mM TCEP, 4 mM Benzamidine-HCl, 1 mg/mL Lysozyme supplemented with 1× cOmplete EDTA-free protease inhibitor (Roche), pH 8.0] by sonication (40% amplitude, six 1-min cycles) and subsequently clarified the lysate by centrifugation at 40,000 rpm in a Ti45 rotor (Beckman Coulter) for 50 min. The supernatant was mixed with Ni-NTA (catalog no. 30250; QIAGEN) at 4 °C for 50 min. The Ni-NTA resin was washed with nickel washing buffer [50 mM phosphate buffer, 20 mM imidazole, 300 mM NaCl, 0.1% Tween-20, 0.5 mM Tris(2-carboxyethyl)phosphine (TCEP), pH 8.0], and then PRC1-SC was eluted with elution buffer (50 mM phosphate buffer, 500 mM imidazole, 100 mM NaCl, 1 mM TCEP, pH 8.0). The fractions containing proteins were pooled, mixed with TEV protease, and dialyzed against 500 mL storage buffer [50 mM phosphate buffer, 300 mM KCl, 20% (wt/vol) sucrose, 10 mM β-mercaptoethanol, pH 8.0] for 12 h. The TEV-digested protein solution was then gel-filtered through Superdex 200 16/60 (catalog no. 28989335; GE Healthcare) that was equilibrated in gel filtration buffer (50 mM Tris, 300 mM KCl, 10 mM β-mercaptoethanol, pH 8.0). Fractions containing PRC1-SC were pooled, mixed with a fivefold volume of low-salt buffer (50 mM Tris, 10 mM β-mercaptoethanol, pH 8.0), and then loaded onto a 1-mL HiTrap SP Sepharose FF column (catalog no. 17-5054-01; GE Life Sciences). Proteins were eluted with a gradient containing 10–100% high-salt buffer (50 mM Tris, 500 mM KCl, 10 mM β-mercaptoethanol, pH 8.0). Fractions containing PRC1-SC were pooled and dialyzed against 1 L storage buffer [50 mM phosphate buffer, 300 mM KCl, 20% (wt/vol) sucrose, 10 mM β-mercaptoethanol, pH 8.0] for 12 h. The purified protein was snap-frozen with liquid nitrogen at a final concentration of 340 μM and stored at −80 °C.

Porcine tubulin (catalog no. T240; Cytoskeleton) was reconstituted to 10 mg/mL in BRB80 buffer [80 mM piperazine-*N*,*N*′-bis (Pipes) (pH 6.9), 1 mM EGTA, 1 mM MgCl$_2$, 1 mM DTT] with 10% (vol/vol) glycerol and 1 mM GTP and was flash-frozen in 5-μL aliquots until needed. Subtilisin (catalog no. P5380; Sigma-Aldrich) was reconstituted to 2 mg/mL in BRB80 buffer with 10% glycerol and was flash-frozen in 5-μL aliquots until needed.

**Cosedimentation Assays.** Equilibrium binding between PRC1-SC and MTs was measured using cosedimentation assays. A 15-μL aliquot of PRC1-SC at 340 μM was diluted to 40 μL in cold BRB80 buffer with 10% glycerol and desalted using a 0.5-mL Zeba column (catalog no. PI89882; VWR). Aggregates were subsequently removed by cold filtration using a spin filter (catalog no. UFC3 0VV 25; Fisher Scientific) and kept at 4 °C. To make dynamic MTs, two 5-μL aliquots of tubulin were thawed, combined, and warmed to 37 °C for 15 min. The MTs were

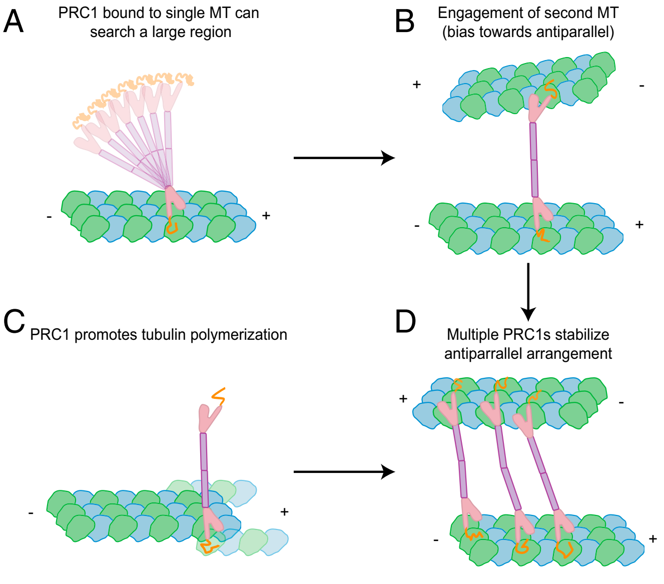

**Fig. 9.** PRC1 flexibility, selectivity for antiparallel MTs, and ability to promote MT polymerization contribute to the formation of stable arrays. (*A*) An isolated PRC1 molecule on an MT can flex significantly to search a large region of space to find an antiparallel MT. (*B*) MTs that are not perfectly antiparallel are biased toward an antiparallel arrangement by PRC1. (*C*) Tubulin polymerization further stabilizes MT regions decorated with PRC1. (*D*) Binding of multiple PRC1 molecules requires MTs to be antiparallel, but PRC1 retains enough flexibility to bind across multiple protofilaments. PRC1 is depicted with the spectrin domain in pink, rod and dimerization domains in purple, and the C-terminal domain in orange. The MT is depicted as three protofilaments with β-tubulin in blue and α-tubulin in green.

pelleted by centrifugation at 17,000 × *g* for 20 min and were resuspended in warm BRB80 buffer with 1 mM GTP and 10% glycerol to a concentration of ∼50 μM. MTs were kept at 37 °C at all times to prevent cold-induced depolymerization.

Taxol/paclitaxel (catalog no. TXD01; Cytoskeleton) was reconstituted to 2 mM in anhydrous DMSO and was frozen in 5-μL aliquots until needed. To make taxol-stabilized MTs, one 5-μL tubulin aliquot was thawed and warmed to 37 °C, and 0.5 μL taxol was added at 10 and 20 min after the tubulin had reached 37 °C. MTs were pelleted as above and resuspended in room-temperature BRB80 buffer with 50 μM taxol.

MTs treated with subtilisin to remove the C-terminal tails of tubulin were prepared by making dynamic or taxol-stabilized MTs, as above, and adding subtilisin to a final concentration of 0.05 mg/mL. Proteolysis was carried out for 20 min at 37 °C. Subtilisin activity was stopped by the addition of PMSF (freshly dissolved in DMSO to 20 mM) to a final concentration of 2 mM in the tubulin proteolysis mixture. Treated MTs were pelleted as above and were resuspended in warm BRB80 buffer with 10% (vol/vol) glycerol and either 1 mM GTP (for dynamic MTs) or 50 μM taxol (for taxol-stabilized MTs). The extent of cleavage was assessed to be 62 ± 2% from the relative intensity of the two tubulin bands clearly separated in the SDS gel following the pelleting assay of the subtilisin-treated taxol-stabilized MTs (Fig. S4). MTs not treated with subtilisin were mock-treated by adding the same volume of subtilisin-free buffer and PMSF at the same time points and also were pelleted a second time.

Protein concentrations for tubulin (after depolymerization by dilution into BRB80 buffer containing 50 mM $CaCl_2$ for taxol-stabilized MTs or cooling on ice for dynamic MTs) and PRC1-SC were measured using absorbance at 595 nm in the presence of Bradford reagent (catalog no. PI-23236; Fisher Scientific). Absorbance values were converted to concentrations using a calibration curve generated using BSA.

For cosedimentation assays with dynamic MTs, tubulin and PRC1-SC were mixed together in BRB80 buffer with 10% glycerol and 1 mM GTP to final concentrations of 10 μM and 5 μM, respectively. Binding reactions were kept at 37 °C at all times. For assays with taxol-stabilized MTs, tubulin and PRC1-SC were mixed together in BRB80 buffer with 10% glycerol and 20 μM taxol at 2 μM and 10 μM, respectively, and were kept at 4 °C to replicate the temperature used when preparing the EM grids. All binding reactions were carried out in 40-μL volumes and were left for 20 min to reach binding equilibrium. The 40-μL binding reaction was layered on top of a 50% glycerol cushion of the same binding buffer and was spun at 310,000 × *g* in a TLA-100 rotor (Beckman Coulter) for 10 min. After centrifugation, the top 45 μL was taken as the supernatant. The middle 70 μL was discarded, and 20 μL of the binding buffer was added to the remaining 25 μL to resuspend the pellet in a volume equal to the supernatant. Then 15 μL of 4× LDS sample buffer (catalog no. NP0007; Life Technologies) supplemented with 80 mM DTT was added to each sample and boiled for 5 min. All the supernatant and the pellet were loaded onto Bolt Bis-Tris 10% polyacrylamide gels (catalog no. NW00100BOX; Life Technologies) and run at 150 V. Gels were stained with SYPRO ruby (catalog no. 170-3125; Bio-Rad) or Flamingo (catalog no. 161-0491; Bio-Rad) overnight and were visualized using a Gel Doc EZ imager (Bio-Rad). Exposure times for gel imaging were adjusted to the longest possible time that did not saturate camera pixels for intense bands to ensure accurate quantitation while maximizing sensitivity for weak bands. Degradation products for PRC1-SC were observed, as reported previously (15). Quantification of protein bands was performed using the built-in Analyze/Gels function of ImageJ (56). A rectangle was drawn covering the protein bands for each lane, and the pixel intensities were integrated within the rectangle for each band to measure the total amount of protein. The raw integrated intensities were used to calculate the fraction of protein in supernatant and pellet fractions for each gel.

**Cryo-EM Sample Preparation and Imaging.** A 10-μL aliquot of PRC1-SC protein was diluted to 50 μL, desalted, and filtered as above, except that glycerol was omitted. A 5-μL aliquot of porcine tubulin was warmed to 37 °C and allowed to polymerize for 15 min. MTs were pelleted by centrifugation at 17,000 × *g* for 20 min and were resuspended in warm EM buffer with 66 μM peloruside A (supplied by John H. Miller and Peter Northcote, Centre for Biodiscovery, Victoria University of Wellington, Wellington, New Zealand).

MTs were diluted to 0.4 mg/mL, and 2 μL of the solution was applied to a glow-discharged C-flat grid with 1.2-μm holes (Protochips). The Mark IV Vitrobot (FEI) used for sample vitrification was set to 4 °C and 100% relative humidity. Maintaining PRC1-SC at low temperature during all experimental procedures minimized protein aggregation and increased occupancy on the MT lattice. MTs were allowed to adhere to the grid for 30 s and then were washed twice with 4 μL of the cold PRC1-SC solution. The grid then was blotted for 4 s with a blot force of 20 Vitrobot units and was plunged into ethane slush.

Images were collected on a Titan electron microscope operated at 300 kV and equipped with a Gatan K2 direct detector (Gatan) using the Leginon automated data-collection pipeline (57). The micrographs have a nominal magnification of 27,500×, resulting in a final pixel size of 1.32 Å per pixel. Twenty frames of 300 ms each were collected at a dose rate of 8 $e^-$ per pixel per second, with a total dose of 28 $e^-/Å^2$.

**Image Analysis and Data Processing.** Images were processed using the Appion pipeline (58), including individual frame alignment using MotionCorr (59) and contrast transfer function estimation using CTFFIND4 (60). Following previous MT reconstruction methods (27), regions of the raw micrographs containing decorated MTs were extracted using overlapping 675-$Å^2$ boxes spaced 80 Å apart. Each of these boxes was treated as an independent, single particle using iterative helical real space reconstruction (IHRSR) (61). The boxed MT segments were sorted by protofilament number, and initial 3D alignment parameters were generated using EMAN2 multimodel refinement (62) with models of 12-, 13-, 14-, and 15-protofilament MTs (63) low-pass filtered to 20-Å resolution, followed by IHRSR using a resolution range of 400–10 Å to obtain initial 3D reconstructions. Frealign (64) was then used to process the 13- and 14-protofilament MTs further to obtain better alignment parameters. Finally, we applied in-house scripts to verify and enforce the seam location (i.e., to align α- and β-tubulin and thus PRC1-SC) for particles from the same MT (28). The overall resolution of the resulting map was not significantly better after this last step, but the protein density for PRC1-SC was notably improved. Local resolution estimates were performed using the Bsoft software package (65) using the whole MT. Half-maps were generated using MT segments separated by MT, rather than even/odd images, to ensure that each half-map did not contain segments from the same MT. The reconstruction was B-factor sharpened (−125 $Å^{-1}$) and low-pass filtered to the estimated overall resolution (4 Å). 2D class averages were obtained by applying the alignment parameters from the 3D reconstruction to the overlapping boxes and averaging them to generate "superparticles" that represent the average of eight boxes and have improved signal. The superparticles were binned by 2 and were subjected to iterative (multivariate statistical analysis/multi-reference alignment) using IMAGIC (66) to generate the final class averages shown in Fig. 1*D* and Fig. S1*B*.

Previous crystallographic structures of PRC1-S [Protein Data Bank (PDB) ID code 3NRX] (15) and of the dimerization, rod, and spectrin domains of PRC1 (PRC1NSΔC, PDB ID code 4L6Y) (26) were used as starting points for our model. Neither structure included the full loop between PRC1 S-H7 and S-H8 (all secondary structures follow the nomenclature established in ref. 26). Initial atomic models of PRC1-SC were generated using the iTASSER server (67), focusing on building this missing loop. Coarse refinement of the predicted structures was performed using iMODFIT (68) to fit the three best starting models from the iTASSER server into the 14-protofilament electron density map. The best model (as judged by agreement with the density) was then refined further using Rosetta (69) to optimize the fit and stereochemistry of the atomic model. The Fourier shell correlation for a simulated map based on this model and the final reconstruction (Fig. 1 and Fig. S1*C*) matches the average local resolution estimates for the PRC1 density and tubulin.

PRC1-SC occupancy was estimated following previously described procedures (27, 28), by comparing the final reconstruction with a simulated map that had 100% PRC1-S occupancy. The simulated map was built by docking heterodimers of tubulin with the bound PRC1-S into the final reconstruction using University of California, San Francisco Chimera (70) for a single protofilament. The molmap command was used to generate electron density for a single protofilament. This density was symmetrized using the same scripts used to generate a whole microtubule during the density refinement. The Fourier transforms for the simulated map and for the final reconstruction were computed using EMAN2 libraries, and the ratio of the amplitudes of the line at the 80-Å layer (and its four higher-order repeats up to 10-Å resolution) on the simulated map and the final reconstruction was used to determine the PRC1-SC occupancy.

**MD Simulations.**

***System preparation***. The starting structures were prepared from the X-ray crystal structure of the PRC1 protein (PDB ID code 4L6Y) (26) using the Protein Preparation Wizard implemented in Maestro, version 9.8 (Schrodinger). This procedure included the modeling of missing side chains and loops using Prime (71). The system was prepared for MD simulations using the GROMACS simulation package version 4.6.3 (72). The Amber99sb-ILDN force field (73) was used for the protein, and the prepared structure was placed in triclinic boxes of explicit TIP3P water molecules (74) with a minimum distance of 20 Å between the protein surface and the border of the box. Some water molecules were replaced with $Mg^{2+}$ ions to neutralize the systems. Additional $Mg^{2+}$ and $Cl^-$ ions were added to reproduce approximately the experimental ion concentration of 1 mM.

***Preparatory simulations*.** The starting structures were energy minimized, and subsequently the solvent was equilibrated in three phases. For the first phase of equilibration, a canonical/NVT (number of particles, volume, and temperature are kept constant) ensemble was applied for 5 ns. Position restraints were applied to all protein atoms using a harmonic potential with a force constant of 1,000 kJ·mol$^{-1}$·nm$^{-2}$. Following NVT, two phases of isothermal–isobaric/NPT (number of particles, pressure, and temperature are kept constant) equilibration were applied for 5 ns each. In the first phase all protein atoms were restrained; in the second phase the position restraint was limited to backbone atoms only. The pressure of the simulation box was kept at an average of the barometric pressure at sea level (1 bar) using the isotropic Berendsen barostat (75) with a time constant of 1 ps and a compressibility of $4.5 \times 10^{-5}$/bar. During the equilibration a 2-fs integrations time-step was used, and the neighbor lists were updated every 10th time-step. Short-range nonbonded van der Waals (Lennard–Jones) and Coulombic interactions were calculated within a cutoff radius of 1.15 nm. The particle mesh Ewald method (76) was used for long-range electrostatic calculations. The long-range Lennard–Jones interactions were analytically corrected for the pressure and the energy calculations. The solvent and the protein were coupled separately to an external heat bath at 300 K with the velocity-rescaling thermostat (77) using a time constant of 0.5 ps. Water molecules were constrained using the SETTLE algorithm (78), and the covalent bonds in the proteins were constrained using the LINCS algorithm (79). Boundaries were treated periodically.

***MD simulations*.** Production MD simulations were carried out for 300 ns using the NPT ensemble in the absence of any restraints. Two replicate simulations were conducted, initiated using different random starting velocities. The isotropic Parrinello–Rahman barostat (80, 81) was used to keep the average pressure at 1 bar with a time constant of 1 ps. All other simulation parameters were the same as the equilibrium simulations. The trajectories were sampled every 80 ps for analysis. In all cases, the simulations reached a steady state, and the integrity of the structure was well maintained over the long-simulation times. Superposition of PRC1 structures at different time points was performed using THESEUS (82).

**Comparisons with Other MT-Binding Domains.** Previous atomic models of motor domains bound to MTs derived from cryo-EM reconstructions (43, 45–47) and crystallography (41) were superimposed on our final atomic model using the H11′ helix on $\alpha$-tubulin to align the binding pockets locally. The following structures were inspected to identify tubulin residues that potentially share binding activity for PRC1, kinesin, or dynein: 2P4N (42), 4HNA (41), 4CK5 (44), 4UXO (45), 3J8Y (46), 3J6P (47), 3J1U, and 3J1T (43). A cutoff distance of 4 Å was used to identify potentially interacting residues.

**Accession Codes.** The atomic coordinates have been deposited in the PDB under the accession code 5KMG. The cryo-EM reconstruction has been deposited in the Electron Microscopy Data Bank under the accession code EMD-8266.

**ACKNOWLEDGMENTS.** We thank Patricia Grob and Tom Houweling for EM and computer support, respectively, and Peter Northcote and John Miller for their generous gift of peloruside. Computational resources for atomic model refinement were provided by the National Energy Research Scientific Computing Center under Grant DE-AC02-05CH11231. This work was supported by National Institute of General Medical Sciences Grants GM051487 (to E.N.) and GM65933 (to T.M.K.) and Ministerio de Economía y Competitividad Grant BFU2013-44306-P (to E.R.-A. and P.C.). The Gauss Centre for Supercomputing/Leibniz Supercomputing Centre provided high-performance computing resources for this project under a Partnership for Advanced Computing in Europe (PRACE) grant. E.N. is a Howard Hughes Medical Institute Investigator.

1. de Forges H, Bouissou A, Perez F (2012) Interplay between microtubule dynamics and intracellular organization. *Int J Biochem Cell Biol* 44(2):266–274.
2. Kapitein LC, Hoogenraad CC (2015) Building the neuronal microtubule cytoskeleton. *Neuron* 87(3):492–506.
3. Brangwynne CP, et al. (2006) Microtubules can bear enhanced compressive loads in living cells because of lateral reinforcement. *J Cell Biol* 173(5):733–741.
4. Hawkins T, Mirigian M, Selcuk Yasar M, Ross JL (2010) Mechanics of microtubules. *J Biomech* 43(1):23–30.
5. Walczak CE, Heald R (2008) Mechanisms of mitotic spindle assembly and function. *Int Rev Cytol* 265(07):111–158.
6. Alfaro-Aco R, Petry S (2015) Building the Microtubule Cytoskeleton Piece by Piece. *J Biol Chem* 290(28):17154–17162.
7. Ward JJ, Roque H, Antony C, Nédélec F (2014) Mechanical design principles of a mitotic spindle. *eLife* 3:e03398.
8. Lee K-Y, Esmaeili B, Zealley B, Mishima M (2015) Direct interaction between centralspindlin and PRC1 reinforces mechanical resilience of the central spindle. *Nat Commun* 6:7290.
9. Akhmanova A, Steinmetz MO (2010) Microtubule +TIPs at a glance. *J Cell Sci* 123(Pt 20): 3415–3419.
10. Blake-Hodek KA, Cassimeris L, Huffaker TC (2010) Regulation of microtubule dynamics by Bim1 and Bik1, the budding yeast members of the EB1 and CLIP-170 families of plus-end tracking proteins. *Mol Biol Cell* 21(12):2013–2023.
11. Goodwin SS, Vale RD (2010) Patronin regulates the microtubule network by protecting microtubule minus ends. *Cell* 143(2):263–274.
12. Jiang K, et al. (2014) Microtubule minus-end stabilization by polymerization-driven CAMSAP deposition. *Dev Cell* 28(3):295–309.
13. Halpain S, Dehmelt L (2006) The MAP1 family of microtubule-associated proteins. *Genome Biol* 7(6):224.
14. Dehmelt L, Halpain S (2005) The MAP2/Tau family of microtubule-associated proteins. *Genome Biol* 6(1):204.
15. Subramanian R, et al. (2010) Insights into antiparallel microtubule crosslinking by PRC1, a conserved nonmotor microtubule binding protein. *Cell* 142(3):433–443.
16. Portran D, et al. (2013) MAP65/Ase1 promote microtubule flexibility. *Mol Biol Cell* 24(12):1964–1973.
17. Stoppin-Mellet V, Fache V, Portran D, Martiel J-L, Vantard M (2013) MAP65 coordinate microtubule growth during bundle formation. *PLoS One* 8(2):e56808.
18. Kosetsu K, de Keijzer J, Janson ME, Goshima G (2013) Microtubule-associated protein65 is essential for maintenance of phragmoplast bipolarity and formation of the cell plate in Physcomitrella patens. *Plant Cell* 25(11):4479–4492.
19. Fourniol FJ, et al. (2014) Micropattern-guided assembly of overlapping pairs of dynamic microtubules. *Methods Enzymol* 540:339–360.
20. Bieling P, Telley IA, Surrey T (2010) A minimal midzone protein module controls formation and length of antiparallel microtubule overlaps. *Cell* 142(3):420–432.
21. Jiang W, et al. (1998) PRC1: A human mitotic spindle-associated CDK substrate protein required for cytokinesis. *Mol Cell* 2(6):877–885.
22. Mollinari C, et al. (2002) PRC1 is a microtubule binding and bundling protein essential to maintain the mitotic spindle midzone. *J Cell Biol* 157(7):1175–1186.
23. Kurasawa Y, Earnshaw WC, Mochizuki Y, Dohmae N, Todokoro K (2004) Essential roles of KIF4 and its binding partner PRC1 in organized central spindle midzone formation. *EMBO J* 23(16):3237–3248.
24. Pellman D, Bagget M, Tu YH, Fink GR, Tu H (1995) Two microtubule-associated proteins required for anaphase spindle movement in Saccharomyces cerevisiae. *J Cell Biol* 130(6):1373–1385.
25. Zhu C, Jiang W (2005) Cell cycle-dependent translocation of PRC1 on the spindle by Kif4 is essential for midzone formation and cytokinesis. *Proc Natl Acad Sci USA* 102(2):343–348.
26. Subramanian R, Ti SC, Tan L, Darst SA, Kapoor TM (2013) Marking and measuring single microtubules by PRC1 and kinesin-4. *Cell* 154(2):377–390.
27. Zhang R, Alushin GM, Brown A, Nogales E (2015) Mechanistic Origin of Microtubule Dynamic Instability and Its Modulation by EB Proteins. *Cell* 162(4):849–859.
28. Zhang R, Nogales E (2015) A new protocol to accurately determine microtubule lattice seam location. *J Struct Biol* 192(2):245–254.
29. Kelley LA, Sternberg MJE (2009) Protein structure prediction on the Web: A case study using the Phyre server. *Nat Protoc* 4(3):363–371.
30. Schlessinger A, Punta M, Yachdav G, Kajan L, Rost B (2009) Improved disorder prediction by combination of orthogonal approaches. *PLoS One* 4(2):e4433, 10.1371/journal.pone.0004433.
31. Barad BA, et al. (2015) EMRinger: Side chain-directed model and map validation for 3D cryo-electron microscopy. *Nat Methods* 12(10):943–946.
32. Garnham CP, et al. (2015) Multivalent microtubule recognition by tubulin tyrosine ligase-like family glutamylases. *Cell* 161(5):1112–1123.
33. Alushin GM, et al. (2012) Multimodal microtubule binding by the Ndc80 kinetochore complex. *Nat Struct Mol Biol* 19(11):1161–1167.
34. Alushin GM, et al. (2014) High-resolution microtubule structures reveal the structural transitions in $\alpha\beta$-tubulin upon GTP hydrolysis. *Cell* 157(5):1117–1129.
35. Alushin GM, et al. (2010) The Ndc80 kinetochore complex forms oligomeric arrays along microtubules. *Nature* 467(7317):805–810.
36. Wilson-Kubalek EM, Cheeseman IM, Milligan RA (2016) Structural comparison of the Caenorhabditis elegans and human Ndc80 complexes bound to microtubules reveals distinct binding behavior. *Mol Biol Cell* 27(8):1197–1203.
37. Baker NA, Sept D, Joseph S, Holst MJ, McCammon JA (2001) Electrostatics of nanosystems: Application to microtubules and the ribosome. *Proc Natl Acad Sci USA* 98(18):10037–10041.
38. Sackett DL, Wolff J (1986) Proteolysis of tubulin and the substructure of the tubulin dimer. *J Biol Chem* 261(19):9070–9076.
39. Lobert S, Correia JJ (1992) Subtilisin cleavage of tubulin heterodimers and polymers. *Arch Biochem Biophys* 296(1):152–160.
40. Nogales E, Zhang R (2016) Visualizing microtubule structural transitions and interactions with associated proteins. *Curr Opin Struct Biol* 37:90–96.
41. Gigant B, et al. (2013) Structure of a kinesin-tubulin complex and implications for kinesin motility. *Nat Struct Mol Biol* 20(8):1001–1007.
42. Sindelar CV, Downing KH (2007) The beginning of kinesin's force-generating cycle visualized at 9-A resolution. *J Cell Biol* 177(3):377–385.
43. Redwine WB, et al. (2012) Structural basis for microtubule binding and release by dynein. *Science* 337(6101):1532–6.
44. Goulet A, et al. (2014) Comprehensive structural model of the mechanochemical cycle of a mitotic motor highlights molecular adaptations in the kinesin family. *Proc Natl Acad Sci USA* 111(5):1837–1842.

45. Atherton J, et al. (2014) Conserved mechanisms of microtubule-stimulated ADP release, ATP binding, and force generation in transport kinesins. *eLife* 3:e03680.
46. Shang Z, et al. (2014) High-resolution structures of kinesin on microtubules provide a basis for nucleotide-gated force-generation. *eLife* 3:e04686.
47. Uchimura S, et al. (2015) A flipped ion pair at the dynein-microtubule interface is critical for dynein motility and ATPase activation. *J Cell Biol* 208(2):211–222.
48. Koonce MP, Tikhonenko I (2000) Functional elements within the dynein microtubule-binding domain. *Mol Biol Cell* 11(2):523–529.
49. Carter AP, et al. (2008) Structure and functional role of dynein's microtubule-binding domain. *Science* 322(5908):1691–1695.
50. Goulet A, et al. (2012) The structural basis of force generation by the mitotic motor kinesin-5. *J Biol Chem* 287(53):44654–44666.
51. Uchimura S, Oguchi Y, Hachikubo Y, Ishiwata S, Muto E (2010) Key residues on microtubule responsible for activation of kinesin ATPase. *EMBO J* 29(7):1167–1175.
52. Kim Y, Holland AJ, Lan W, Cleveland DW (2010) Aurora kinases and protein phosphatase 1 mediate chromosome congression through regulation of CENP-E. *Cell* 142(3):444–455.
53. Zimniak T, Stengl K, Mechtler K, Westermann S (2009) Phosphoregulation of the budding yeast EB1 homologue Bim1p by Aurora/Ipl1p. *J Cell Biol* 186(3):379–391.
54. Wilson-Kubalek EM, Cheeseman IM, Yoshioka C, Desai A, Milligan RA (2008) Orientation and structure of the Ndc80 complex on the microtubule lattice. *J Cell Biol* 182(6):1055–1061.
55. Dumont S, Mitchison TJ (2009) Force and length in the mitotic spindle. *Curr Biol* 19(17):R749–R761.
56. Schneider CA, Rasband WS, Eliceiri KW (2012) NIH Image to ImageJ: 25 years of image analysis. *Nat Methods* 9(7):671–675.
57. Suloway C, et al. (2005) Automated molecular microscopy: The new Leginon system. *J Struct Biol* 151(1):41–60.
58. Lander GC, et al. (2009) Appion: An integrated, database-driven pipeline to facilitate EM image processing. *J Struct Biol* 166(1):95–102.
59. Li X, et al. (2013) Electron counting and beam-induced motion correction enable near-atomic-resolution single-particle cryo-EM. *Nat Methods* 10(6):584–590.
60. Rohou A, Grigorieff N (2015) CTFFIND4: Fast and accurate defocus estimation from electron micrographs. *J Struct Biol* 192(2):216–221.
61. Egelman EH (2007) The iterative helical real space reconstruction method: Surmounting the problems posed by real polymers. *J Struct Biol* 157(1):83–94.
62. Tang G, et al. (2007) EMAN2: An extensible image processing suite for electron microscopy. *J Struct Biol* 157(1):38–46.
63. Sui H, Downing KH (2010) Structural basis of interprotofilament interaction and lateral deformation of microtubules. *Structure* 18(8):1022–1031.
64. Lyumkis D, Brilot AF, Theobald DL, Grigorieff N (2013) Likelihood-based classification of cryo-EM images using FREALIGN. *J Struct Biol* 183(3):377–388.
65. Heymann JB, Belnap DM (2007) Bsoft: Image processing and molecular modeling for electron microscopy. *J Struct Biol* 157(1):3–18.
66. van Heel M, Harauz G, Orlova EV, Schmidt R, Schatz M (1996) A new generation of the IMAGIC image processing system. *J Struct Biol* 116(1):17–24.
67. Roy A, Kucukural A, Zhang Y (2010) I-TASSER: A unified platform for automated protein structure and function prediction. *Nat Protoc* 5(4):725–738.
68. Lopéz-Blanco JR, Chacón P (2013) iMODFIT: Efficient and robust flexible fitting based on vibrational analysis in internal coordinates. *J Struct Biol* 184(2):261–270.
69. DiMaio F, et al. (2015) Atomic-accuracy models from 4.5-Å cryo-electron microscopy data with density-guided iterative local refinement. *Nat Methods* 12(4):361–365, 10.1038/nmeth.3286.
70. Pettersen EF, et al. (2004) UCSF Chimera–a visualization system for exploratory research and analysis. *J Comput Chem* 25(13):1605–1612.
71. Jacobson MP, et al. (2004) A hierarchical approach to all-atom protein loop prediction. *Proteins* 55(2):351–367.
72. Hess B, Kutzner C, van der Spoel D, Lindahl E (2008) GROMACS 4: Algorithms for Highly Efficient, Load-Balanced, and Scalable Molecular Simulation. *J Chem Theory Comput* 4(3):435–447.
73. Hornak V, et al. (2006) Comparison of multiple Amber force fields and development of improved protein backbone parameters. *Proteins* 65(3):712–725.
74. Jorgensen WL, Chandrasekhar J, Madura JD, Impey RW, Klein ML (1983) Comparison of simple potential functions for simulating liquid water. *J Chem Phys* 79(2):926–935.
75. Berendsen HJC, Postma JPM, van Gunsteren WF, DiNola A, Haak JR (1984) Molecular dynamics with coupling to an external bath. *J Chem Phys* 81(8):3684–3690.
76. Essmann U, et al. (1995) A smooth particle mesh Ewald method. *J Chem Phys* 103: 8577–8593.
77. Bussi G, Donadio D, Parrinello M (2007) Canonical sampling through velocity rescaling. *J Chem Phys* 126(1):014101.
78. Miyamoto S, Kollman PA (1992) SETTLE: An analytical version of the SHAKE and RATTLE algorithm for rigid water models. *J Comput Chem* 13(8):952–962.
79. Hess B, Bekker H, Berendsen HJC, Fraaije JGEM (1997) LINCS: A linear constraint solver for molecular simulations. *J Comput Chem* 18(12):1463–1472.
80. Parrinello M, Rahman A (1981) Polymorphic transitions in single crystals: A new molecular dynamics method. *J Appl Phys* 52(12):7182–7190.
81. Nosé S, Klein ML (1983) Constant pressure molecular dynamics for molecular systems. *Mol Phys* 50(5):1055–1076.
82. Theobald DL, Wuttke DS (2006) THESEUS: Maximum likelihood superpositioning and analysis of macromolecular structures. *Bioinformatics* 22(17):2171–2172.

# Supporting Information

**Kellogg et al. 10.1073/pnas.1609903113**

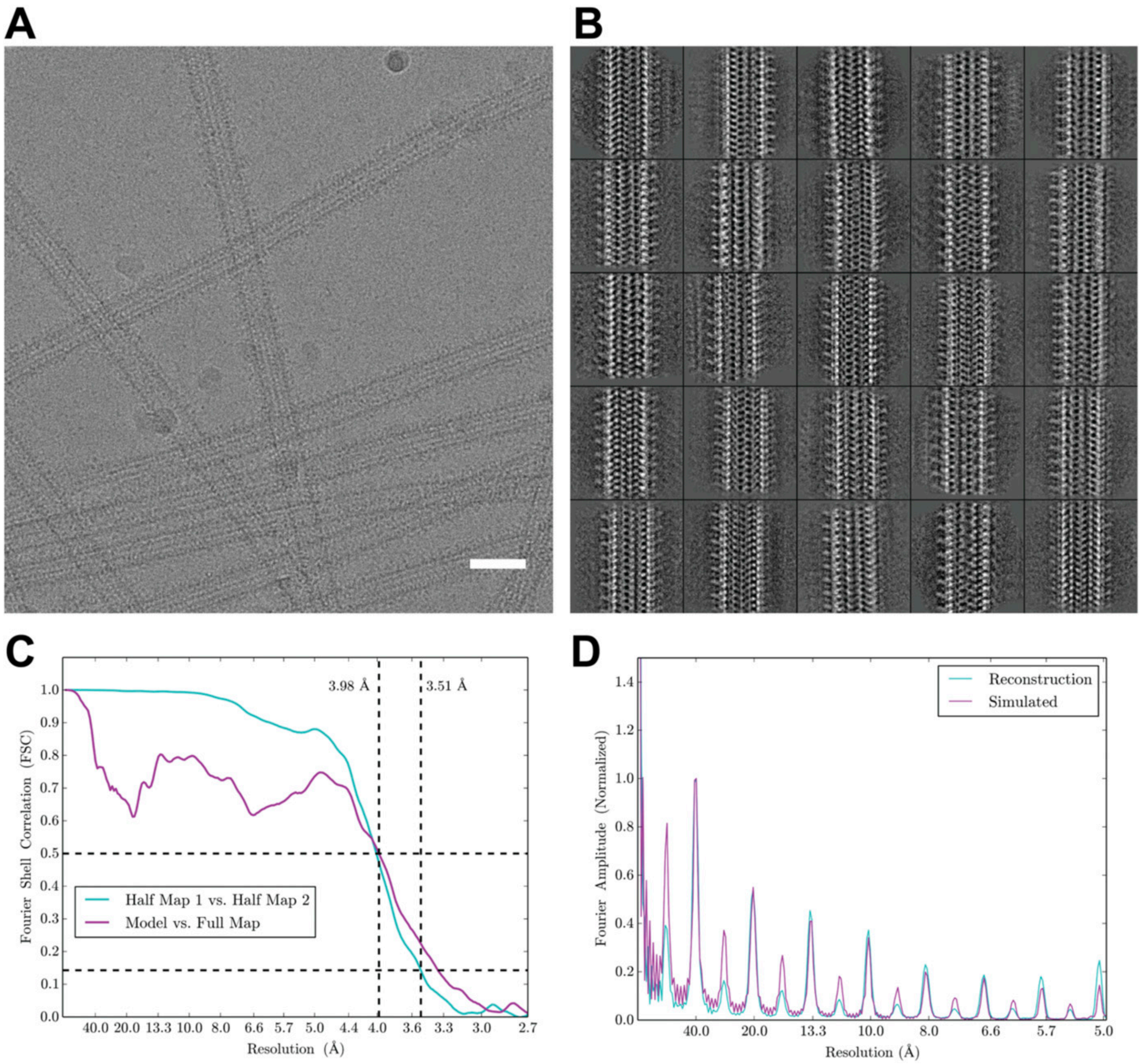

**Fig. S1.** Cryo-EM data and analysis. (*A*) Raw micrograph of peloruside-stabilized MTs decorated with PRC1-SC. (Scale bar: 50 nm.) (*B*) 2D class averages of microtubules decorated with PRC1-SC. (*C*) Fourier shell correlation between volumes reconstructed using half sets of the data (cyan) and between the final atomic model for tubulin–PRC1-SC and the final decorated dimer density (purple). (*D*) Fourier amplitudes of the final reconstruction (cyan) and the simulated map (purple) used to estimate PRC1-SC occupancy on the MT lattice.

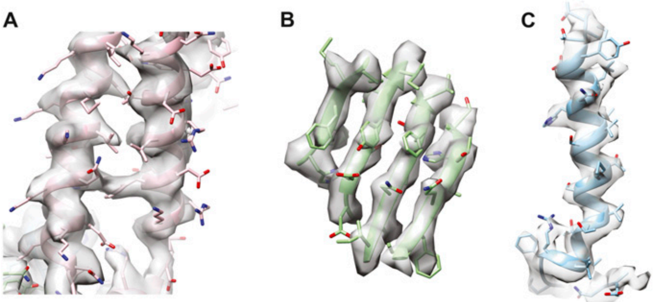

**Fig. S2.** High-resolution features of the cryo-EM reconstruction. (*A*) Helix S-H7 of PRC1 shows clear density for large aromatic side chains as well as smaller hydrophobic side chains. (*B*) β-Strands in α-tubulin are clearly separated, and side-chain density is clearly visible. (*C*) Helix H7 of β-tubulin shows side-chain density clearly.

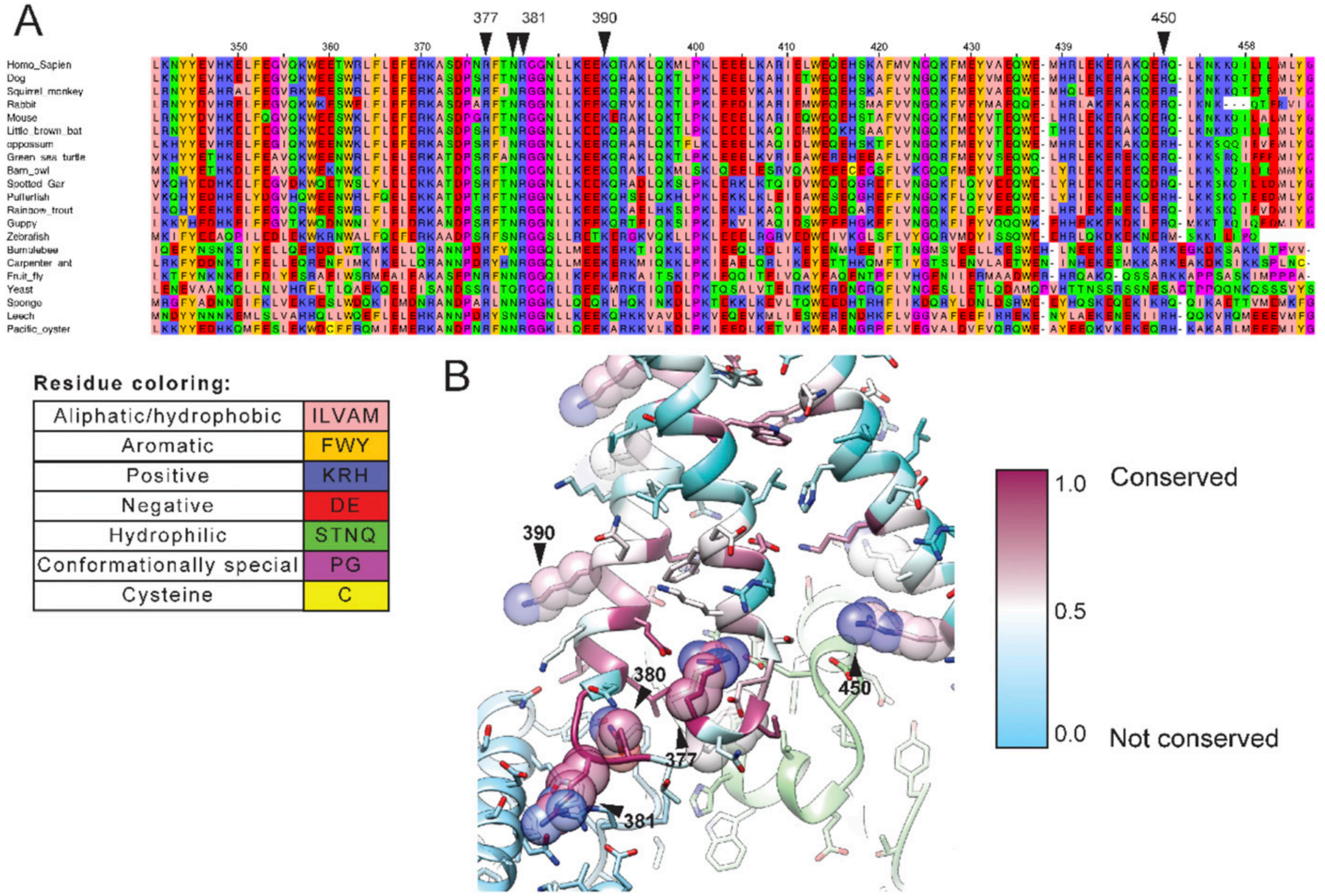

**Residue coloring:**

| | |
|---|---|
| Aliphatic/hydrophobic | ILVAM |
| Aromatic | FWY |
| Positive | KRH |
| Negative | DE |
| Hydrophilic | STNQ |
| Conformationally special | PG |
| Cysteine | C |

**Fig. S3.** Sequence conservation of key residues for MT interaction with PRC1. (*A*) Sequences across eukaryotic species for the spectrin domain of PRC1. Amino acids are colored according to biochemical property (hydrophobicity, aromatic, charge, and special amino acids). Residues observed to be interacting with the MT (marked by arrowheads above the panel) are highly conserved; numbering shown is according to human PRC1. (*B*) PRC1-S is colored according to sequence conservation; highly conserved positions are colored maroon, and poorly conserved positions are colored cyan. Highlighted residues that interact with tubulin are shown as spheres.

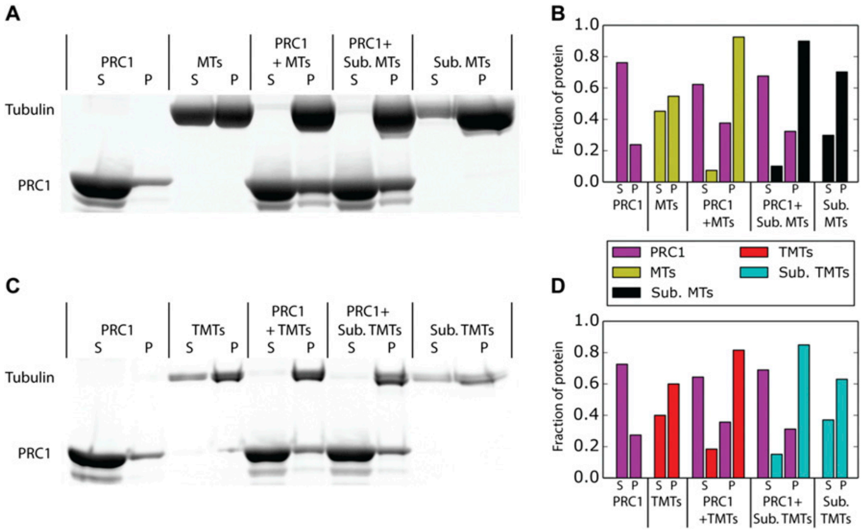

**Fig. S4.** PRC1-SC promotes tubulin polymerization into dynamic and taxol-stabilized MTs and does not require the C-terminal tails of tubulin. SDS/PAGE analysis of cosedimentation assays showing supernatant (S) and pellet (P) fractions for PRC1-SC bound to dynamic MTs (MTs) and subtilisin-treated dynamic MTs (Sub. MTs), tubulin at 10 μM and PRC1-SC at 5 μM (*A*) (quantitation in *B*) and taxol-stabilized MTs (TMTs) and subtilisin-treated taxol MTs (Sub. TMTs), tubulin at 2 μM and PRC1-SC at 10 μM (*C*) (quantitation in *D*). More tubulin in the pellet fractions in the presence of PRC1-SC for dynamic and taxol-stabilized MTs shows increased tubulin polymerization for untreated and subtilisin-treated MTs. Note the tubulin concentration for dynamic MTs is fivefold higher than for taxol MTs. Brightness and contrast of gels were adjusted to visualize weak bands.

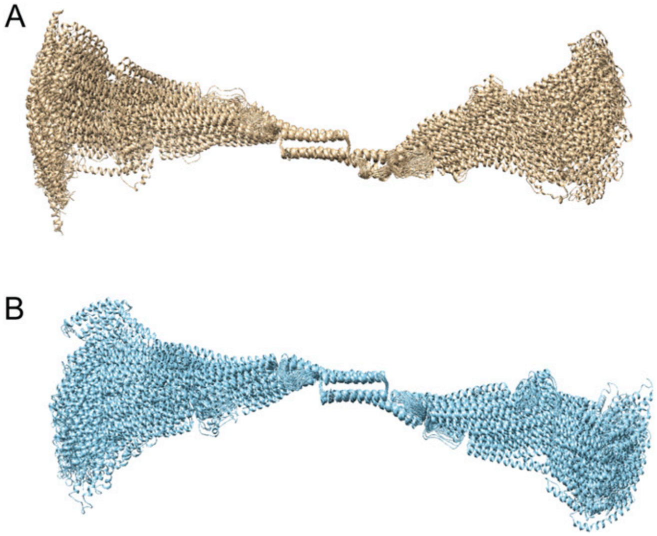

**Fig. S5.** The PRC1 dimer is flexible and adopts a range of conformations. Structures from the final 100 ns of two MD trajectories (*A* and *B*) aligned by a maximum-likelihood superimposition criterion show significant flexibility of the molecule and rotation of the spectrin domains.

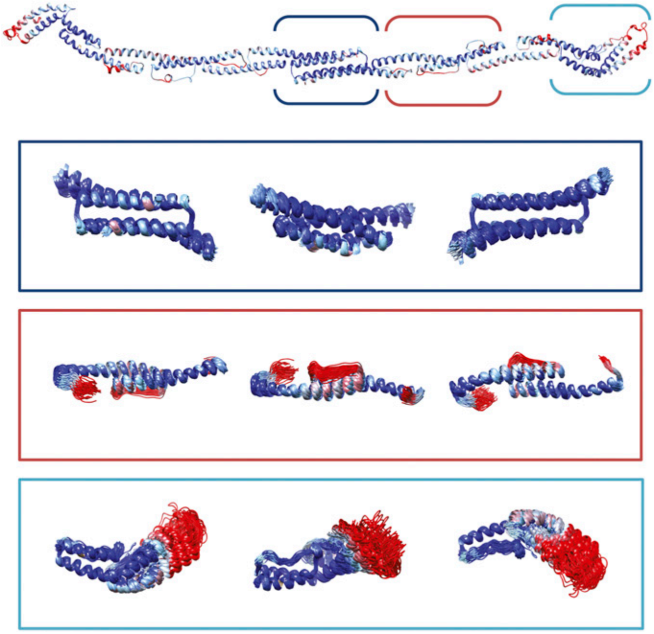

**Fig. S6.** PRC1 homodimer colored by the relative root mean square fluctuation deviation found in the last 100 ns of the simulation. (*Top*) The lowest deviations were found at the dimerization domain (dark blue box, residues 7–70 in blue) and at the junction between the rod and spectrin domains (cyan box, residues 290–360 in blue). The rod domain is the most flexible part the molecule triggered by multiple flexible joints located mainly in loop regions. Nevertheless, the structural modules of the rod domain are well conserved during the simulations (red box, residues 88–193). The tips of the spectrins also exhibited a high degree of flexibility (cyan box, residues 361–400 in red). (*Middle* and *Bottom* boxes) Each box, corresponding to the three elements marked with the same color parentheses on the top, shows three orthogonal views (rotating around the *x* axis by 90°) of the local alignment of the characteristic structural regions from the structures of final 100 ns of the two MD trajectories. The alignment was performed using THESEUS.

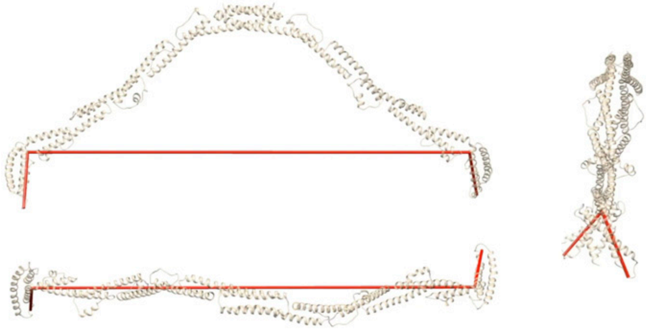

**Movie S1.** Illustrative MD simulation trajectory of PRC1 showing three orthogonal views of the protein dynamics during the entire 300-ns simulation time.

Movie S1